



Epigenetic Control of *Cdkn2a.Arf* Protects Tumor-Infiltrating Lymphocytes from Metabolic Exhaustion

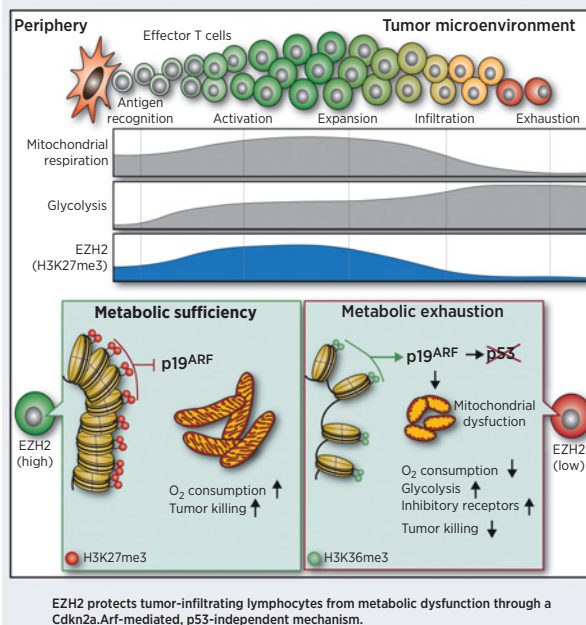
Brian Koss¹, Bradley D. Shields¹, Erin M. Taylor¹, Aaron J. Storey¹, Stephanie D. Byrum^{1,2,3}, Allen J. Gies^{1,3}, Charity L. Washam^{1,3}, Samrat Roy Choudhury¹, Jeong Hyun Ahn⁴, Hidetaka Uryu⁴, Jason B. Williams⁵, Kimberly J. Krager⁶, Tung-Chin Chiang⁷, Samuel G. Mackintosh¹, Rick D. Edmondson², Nukhet Aykin-Burns⁶, Thomas F. Gajewski⁵, Gang Greg Wang⁴, and Alan J. Tackett^{1,2,3}

ABSTRACT

T-cell exhaustion in cancer is linked to poor clinical outcomes, where evidence suggests T-cell metabolic changes precede functional exhaustion. Direct competition between tumor-infiltrating lymphocytes (TIL) and cancer cells for metabolic resources often renders T cells dysfunctional. Environmental stress produces epigenome remodeling events within TIL resulting from loss of the histone methyltransferase EZH2. Here, we report an epigenetic mechanism contributing to the development of metabolic exhaustion in TIL. A multiomics approach revealed a *Cdkn2a.Arf*-mediated, p53-independent mechanism by which EZH2 inhibition leads to mitochondrial dysfunction and the resultant exhaustion. Reprogramming T cells to express a gain-of-function EZH2 mutant resulted in an enhanced ability of T cells to inhibit tumor growth *in vitro* and *in vivo*. Our data suggest that manipulation of T-cell EZH2 within the context of cellular therapies may yield lymphocytes that are able to withstand harsh tumor metabolic environments and collateral pharmacologic insults.

Significance: These findings demonstrate that manipulation of T-cell EZH2 in cellular therapies may yield cellular products able to withstand solid tumor metabolic-deficient environments.

Graphical Abstract: <http://cancerres.aacrjournals.org/content/canres/80/00/000/F1.large.jpg>.



¹Department of Biochemistry and Molecular Biology, University of Arkansas for Medical Sciences, Little Rock, Arkansas. ²Winthrop P. Rockefeller Cancer Institute, University of Arkansas for Medical Sciences, Little Rock, Arkansas. ³Arkansas Children's Research Institute, Little Rock, Arkansas. ⁴Lineberger Comprehensive Cancer Center, Department of Biochemistry and Biophysics, University of North Carolina at Chapel Hill School of Medicine, Chapel Hill, North Carolina. ⁵Department of Pathology, The University of Chicago, Chicago, Illinois. ⁶Department of Pharmaceutical Sciences, College of Pharmacy, University of Arkansas for Medical Sciences, Little Rock, Arkansas. ⁷Department of Environmental and Occupational Health, University of Arkansas for Medical Sciences, Little Rock, Arkansas.

Note: Supplementary data for this article are available at Cancer Research Online (<http://cancerres.aacrjournals.org/>).

Corresponding Author: Alan J. Tackett, University of Arkansas for Medical Sciences, 4301 W Markham St Slot 516, Little Rock, AR 72205. Phone: 501-686-8152; Fax: 501-686-8169; E-mail: ajtackett@uams.edu

Cancer Res 2020;XX:XX-XX

doi: 10.1158/0008-5472.CAN-20-0524

©2020 American Association for Cancer Research.

Introduction

The ability of the immune system to sustain T-cell function in a wide range of environments provides the immunosurveillance necessary to eliminate genetically damaged cells, protecting the host from developing overt malignancies. Cancer cells that escape the initial immune response can form solid tumors, which undergo further immunoeediting, driving the generation of an immunosuppressive microenvironment, resulting in restricted T-cell infiltration and effector function (1). Features of the immune-hostile tumor environment include direct repression and recruitment of immunosuppressive cell populations, culminating in failure of the antitumor immune response and disease progression (2, 3). The continuous T-cell activation signaling in sustained antitumor responses promotes expression of inhibitory receptors (PD-1, CTLA-4, Tim-3, and LAG-3), which negatively regulate activation and effector functions, resulting in intrinsically driven T-cell exhaustion programs. Importantly, T cells can still display an exhausted phenotype in the absence of inhibitory molecules (4). In the context of solid tumors, one driving force of T-cell exhaustion results from inhibitory metabolic parameters encountered

by tumor-infiltrating lymphocytes (TIL) such as glucose deprivation and mitochondrial dysfunction (5, 6). Recent discoveries have highlighted various metabolic pathways as key intrinsic mechanisms through which T cells regulate their fate (7, 8). Nutrient availability is a primary driver of metabolic programming and is a necessary signal for maintenance of self-tolerance and protecting the host from tissue damage (9, 10). Loss of T-cell metabolic regulatory signals can be illustrated by the strong correlation between metabolic syndrome (obesity, hyperglycemia, dyslipidemia, and hypertension) and autoimmune diseases (11). T cells, like cancer cells, primarily utilize aerobic glycolysis for their energy needs. However, mitochondria are critical organelles for maintaining the integrity of effector T cells and the formation of memory T cells (12). TILs show a progressive loss of mitochondrial function and a reduction in glucose uptake (metabolic exhaustion), which is largely independent of checkpoint blockade or regulatory cell suppression (13).

Recent studies have begun to highlight the metabolic underpinnings of T-cell function and raised the possibility of metabolic manipulation aimed at vastly improving cancer immunotherapy (14, 15). The dynamic interplay between epigenetics and metabolic pathways has been revealed as primary mechanism cells use to sense and respond to environmental pressures (16). One such metabolic and epigenetic circuit is observed when T cells experience glucose deprivation and downregulate the epigenetic modifier, EZH2. During T-cell activation, EZH2 is rapidly upregulated and tumor-induced glucose deprivation suppresses EZH2 function, resulting in an overtly immunosuppressive environment (17). EZH2 is a histone methyltransferase that functions as the catalytic subunit of the polycomb-repressive complex-2 (PRC2). The PRC2 complex represses genes through methylation events (di- and trimethylation) of Lysine-27 on histone 3 (18). The trimethylation state, H3K27me3, is associated with long-term transcriptional repression. Importantly, misregulation of EZH2 in cancer has led to the development of inhibitors, which have been proposed for combination with immunotherapies (19, 20). However, the role of EZH2 in T-cell function must be a therapeutic consideration, as the hostile metabolic environment of solid tumors innately drives EZH2 suppression within T cells, which would only be furthered by systemic EZH2 inhibitor therapy. EZH2^{high} CD8⁺ T cells are associated with improved T-cell function, providing clear rationale for mitigating anti-EZH2 effects, whether from anticancer therapies or those intrinsic to the metabolic environment T-cell face within solid tumors (17, 21, 22). Here, we seek to characterize the relationship between the loss of EZH2 and metabolic stress-induced exhaustion in T cells.

Materials and Methods

Mouse models

The C57BL/6 (stock #000664), CD45.1:B6.SJL-Ptprca Pepcb/BoyJ (stock # 002014), Arf-KO:B6.129 × 1-Cdkn2atm1Cjs/KaiJ (stock# 029676), Rag1-KO: B6.129S7-Rag1tm1Mom/J (stock#), and the MHC class I-restricted OVA-specific TCR OT-I: C57BL/6-Tg(TcrαTcrβ) 1100Mjb/J mice were purchased from The Jackson laboratory. The Lck-EZH2^{Y641F} transgenic mice were provided as a gift by Dr. Keith Humphries (BC Cancer Agency, British Columbia, Canada) and screened by PCR prior to experimentation. The animal experiments described in this study were reviewed and approved by the University of Arkansas for Medical Sciences Institutional Animal Care and Use Committee. Mice were bred pathogen-free standards and transferred to open top cages for experimental procedures. For tumor experiments, 8- to 15-week-old mice were randomized to match age and

gender across experimental groups. No association of sex or weight with response was observed or expected.

Tumor challenge

Mice were injected in the subcutaneous flank space with 1×10^6 tumor cells suspended in 100 μ L of PBS. Tumor growth was monitored daily with caliper measurements of tumor length and width. Survival was plotted on Kaplan–Meier curves, the number of days after tumor engraftment where the tumor was less than 1,000 mm³ (unless noted differently), with no ulceration. Tumor challenge studies were performed in all cases at least twice. For *in vivo* EZH2i, starting on day 5, mice were injected (orally) with vehicle (0.5% w/v methyl cellulose and 0.1% Tween-80) or 250 mg/kg tazemetostat (EPZ6438) twice daily for 5 consecutive days.

Primary cell culture

Naïve lymphocytes (CD8⁺, CD4⁺, or CD4⁺CD25⁺) were isolated from single-cell suspension of murine splenocytes using magnetic selection (Miltenyi). Purified lymphocytes were then activated using 5 μ g/mL of plate-bound antiCD3e (Biolegend), 2 μ g/mL soluble CD28 (Biolegend) and 50 U/mL IL2 (Peprotech) for indicated times. Lymphocytes were cultured in RPMI (Life Technologies) with 10% FBS, 55 μ mol/L 2-mercaptoethanol, 2 mmol/L glutamine, penicillin, and streptomycin at 37°C and 5% CO₂.

Cell lines

The B16F10 mouse cell line was purchased from the ATCC. The B16^{SIY} cell line was a kind gift from Thomas F. Gajewski (University of Chicago). Tumor cell lines were cultured in DMEM supplemented with 10% FBS, penicillin, and streptomycin at 37°C and 5% CO₂. All tumor cell lines were screened for contaminating pathogens (Ectromelia, EDIM, LCMV, MAV1, MAV2, MHV, MPV, MVM, Mycoplasma pulmonis, Polyoma, PVM, REO3, Sendai, TMEV) by IDEXX laboratories and do not contain any pathogens or *Mycoplasma*.

Generation of MC38^{SIINFEKL}

MC38 cells were engineered to express DsRed fused in frame with three repeated sequences encoding the model antigen SIINFEKL followed by an AAY linker. The construct was generated by digesting a gBlock (IDT) encoding 3X-SIINFEKL-AAY with flanking XhoI/BamHI cut sites. Note that 100 ng of the gBlock and 1 μ g of pRetro-dsRed-monomer-N1 (Takara: 632465) were digested with XhoI and BamHI and gel purified (QIAGEN). Purified digested gBlock and pRetro vectors were ligated together and transformed into Stbl3 (Fisher) cells. The insert region of the pRetro-SIINFEKL-dsRed vector was sequenced to confirm that the insert was in-frame with dsRed without intervening stop codons. To generate the MC38.SIINFEKL-dsRed cell line, Phoenix (ATCC) cells were transfected with the pRetro-SIINFEKL-dsRed vector using Lipofectamine 3000 (Fisher) following the manufacturer's protocol. Forty-eight hours after transfection, supernatant was collected, filtered through a 0.45 μ m filter, and added to tumor cells with polybrene at 10 μ g/mL. After expansion, cells were sorted based on dsRed expression. The cells were sorted 3 more times for the top 5% dsRed positive to ensure no dsRed cells remained.

IFN γ ELISPOT assay

Mice were injected in the subcutaneous flank space with 1×10^6 tumor cells suspended in 100 μ L of PBS. Spleens were harvested 7 days after injection for analysis. The enzyme-linked Immunospot assay (ELISPOT) was conducted with the BD mouse IFN γ kit according to the manufacturer's protocol. Splenocytes were plated at 10⁶ cells/well

and stimulated overnight with SIINFEKL peptide (160 nmol/L), or PMA (50 ng/mL) and ionomycin (0.5 μ mol/L). IFN γ spots were detected using biotinylated antibody and avidin-peroxidase and developed using AEC substrate (Sigma-Aldrich).

In vitro killing assay

T-cell killing assays were carried out using preactivated CD8⁺ T cells from wt (control) or OT-1 (tumor-specific) mice. Activated T cells were washed and labeled with Cell Trace violet to enable their subsequent discrimination from target cells. Target cells (MC38^{SIINFEKL}) were plated for 16 hours prior to culturing with T cells. The cocultures were conducted at different target: effector (T:E) ratios for 10 hours. Target cell viability was then determined by the percentage of Annexin V and propidium iodide (PI) cells.

Adoptive transfers

For *in vivo* survival experiments, 2×10^6 activated CD8⁺ T cells/mouse were injected i.v. into CD45.1⁺ C57BL/6 mice. Cells were recovered 2 days later from the peripheral blood, spleen, and lymph nodes and then analyzed by flow cytometry. For adoptive cellular treatment experiments, 4×10^6 CD8⁺ OT-I⁺ or CD8⁺ OT-I⁺ Lck-EZH2⁺ preactivated T cells/mouse were injected i.v. into tumor-bearing (MC38^{SIINFEKL}) mice and measured for tumor volume growth.

Western blotting and quantitative PCR

For immunoblot analysis, harvested cells were lysed on ice for 30 minutes with RIPA (10 mmol/L Tris-Cl (pH 8.0), 1 mmol/L EDTA, 0.5 mmol/L EGTA, 1% Triton X-100, 0.1% sodium deoxycholate, 0.1% SDS, 140 mmol/L NaCl). Lysates were then cleared by centrifugation, and protein concentrations were determined by bicinchoninic acid protein assay (Thermo). Electrophoresis was performed using bis-Tris gels 4%–12% (Invitrogen) and then samples were transferred to polyvinylidene difluoride (Millipore) membranes. Detection was performed using Western Lightning Plus ECL enhanced chemiluminescent substrate (Perkin-Elmer) according to the manufacturer's instructions. See Supplementary Methods for the information of antibodies used.

For QPCR, RNA was extracted from activated lymphocytes using an RNAeasy purification kit (Qiagen), and complementary DNA was synthesized (Bio-Rad). Target Primer sets below were used with Sybr-Green (Bio-Rad) to measure relative transcript levels. Ubiquitin was used as a house keeping gene. $\Delta\Delta$ CT was used to calculate relative fold change.

FACS and TIL sort

Mitochondrial dyes

Mitochondrial mass was analyzed using Mitotraker Green FM (Thermo) at 100 nmol/L according to the manufacturer's protocol. Mitochondrial membrane potential was analyzed using tetramethylrhodamine methyl ester (TMRM; Thermo) at 50 nmol/L according to the manufacturer's protocol. Mitochondrial superoxide was analyzed using MitoSOX at 1 μ mol/L according to the manufacturer's protocol.

Cell cycle was analyzed by fixing cells in 70% ethanol overnight and staining with PI/RNase Staining Buffer (BD Biosciences). FACS data were analyzed with Flow Jo/Dean-Jett Fox model (BD Biosciences).

TIL purification

Tumor dissociation was performed using mechanical separation and was resuspended in FACs Buffer (PBS with 1% FBS) at 1×10^6 cells/100 μ L and blocked with FcBlocker (BD Biosciences). The following antibodies were used to define immune

populations: anti-CD3 (Biolegend), anti-CD45, anti-CD19, anti-CD8, anti-CD4, anti-CD11b, anti-Gr1, and anti-NK1.1. DAPI was used as a viability stain. For cell sorting tumors, dead cells were depleted prior to staining using dead cell removal magnetic beads (Miltenyi). FACSAria was used for cell sorting.

EM imaging

T cells were harvested and then fixed for 2 hours at room temperature with 2.5% glutaraldehyde and 0.05% malachite green in 0.1 mol/L sodium cacodylate buffer, pH 6.8. Samples were postfixed for 30 minutes with 0.5% osmium tetroxide and 0.8% potassium ferricyanide in 0.1 mol/L sodium cacodylate, for 1 hour in 1% tannic acid, and for 1 hour in 1% uranyl acetate at room temperature. Specimens were dehydrated with a graded ethanol series and embedded in resin. Thin sections were cut with an RMC MT-7000 ultramicrotome (Ventana) stained with 1% uranyl acetate and lead citrate before viewing at 200 keV on a FEI Tecnai F20 Transmission Electron Microscope. Digital images were acquired with an AMT digital camera system (23).

Metabolic phenotyping

Extracellular acidification rate (ECAR) and oxygen consumption rate (OCR) were measured using the Seahorse XFe bioanalyzer. Note that 2×10^5 T cells per well (≥ 8 wells per sample) were spun onto Cell-Tak (Corning)-coated seahorse 96-well plates and preincubated at 37°C for approximately 20 minutes in the absence of CO₂. OCR and ECAR were measured in XF media (nonbuffered RPMI 1640 containing 10 mmol/L glucose, 2 mmol/L L-glutamine, and 1 mmol/L sodium pyruvate) under basal conditions and in response to 2 μ mol/L oligomycin, 2 μ mol/L fluoro-carbonyl cyanide phenylhydrazone (FCCP), 10 mmol/L 2-Deoxy-D-glucose, and 500 nmol/L rotenone + 500 nmol/L antimycin A.

ATP measurements

Relative ATP levels were determined using Cell titer Glo (Promega) according to the manufacturer's protocol. Note that 1×10^5 activated T cells were used per 96 well to determine relative luminescence unit for each condition.

Cell death experiments

Activated CD8⁺ lymphocytes were plated in fresh media at 0.5×10^6 cells/mL in 96-well plates. Cells were treated with glucose or glutamine withdrawal, H₂O₂ (Sigma), 2-DeoxyGlucose (Sigma), Staurosporine (Seleckchem), or vehicle control at indicated doses for 24 hours. Cell viability was determined by staining with Annexin V-FITC and DAPI staining. For withdrawal of glucose and glutamine, cells were cultured in dialyzed FBS.

Histone mass spectrometry and post-translational modification identification

Histone mass spectrometry was carried out as described previously (24). Histones were purified by acid extraction and resolved on a 4%–12% gradient SDS-PAGE gel. Histone bands were visualized by Coomassie staining. Histones were excised from the gel, destained, and treated with 20 μ L/band of 30% D6-acetic anhydride in 50 mmol/L ammonium bicarbonate, which chemically adds isotopically heavy acetylation on unmodified and monomethylated lysines. Histones were then digested in-gel with 125 ng/band sequencing-grade trypsin at 37°C for overnight. Acidified tryptic peptides were separated using a 2.5 μ m Waters XSelect CSH resin on a 150 mm X 0.075 mm column using a nanoAcquity UPLC system (Waters). Peptides were separated with a 60-minute chromatography gradient, with a 40-minute linear

separation gradient from 97% buffer A [0.1% formic acid in water (v/v)], 3% buffer B [0.1% formic acid (v/v), 99.9% acetonitrile (v/v)], to 80% of buffer A, 20% buffer B. Eluted peptides were ionized by electrospray (2,150 V) and analyzed on an Orbitrap Fusion Lumos mass spectrometer (Thermo) using data-dependent acquisition. Spectral count data were exported in tabular format and analyzed using R. Additional details regarding histone mass spectrometry and post-translational modification (PTM) identification are available in the Supplementary Materials.

FASP bHPLC TMT mass spectrometry

Purified proteins were reduced, alkylated, and digested using filter-aided sample preparation (25). Tryptic peptides were separated into 36 fractions on a 100×1.0 mm Acquity BEH C18 column (Waters) using an UltiMate 3000 UHPLC system (Thermo) with a 40-minute gradient from 99:1 to 60:40 buffer A:B ratio under basic pH conditions, and then consolidated into 12 superfractions. Each superfraction was then further separated by reverse phase Jupiter Proteo resin (Phenomenex) on an in-line 200×0.075 mm column using a nanoAcquity UPLC system (Waters). Peptides were eluted using a 60-minute gradient from 97:3 to 67:33 buffer A:B ratio. Eluted peptides were ionized by electrospray (2.15 kV) followed by mass spectrometric analysis on an Orbitrap Fusion Tribrid mass spectrometer (Thermo) using multi-notch MS3 parameters. Scaffold Q+S (Proteome Software) was used to verify MS/MS-based peptide and protein identifications (protein identifications were accepted if they could be established with less than 1.0% false discovery and contained at least 2 identified peptides; protein probabilities were assigned by the Protein Prophet algorithm and to perform reporter ion-based statistical analysis; ref. 26). Additional details regarding TMT mass spectrometry are available in the Supplementary Materials.

RNA sequencing

RNA sequencing (RNA-seq) was carried out as before (27). For total RNA-seq, the Sequence library was prepared from 500 ng of total RNA using Illumina's TruSeq RNA Sample Preparation Kit v2 following the manufacturer's protocol. cDNA Libraries were validated on the Arkansas Children's Research Institute Genomics core Fragment Analyzer for fragment size peak of approximately 260 bp and were quantified by a Qubit fluorometer. Equal amounts of each library were pooled for sequencing on the NextSeq 500 platform using a high output flow cell to generate approximately 25 million 75-base reads per sample. cDNA libraries were constructed using Illumina's TruSeq stranded mRNA sample preparation kit according to the manufacturer's protocol. All sequencing was conducted by the Center for Translational Pediatric Research Genomics Core Lab at Arkansas Children's Research Institute (Little Rock, AR). For each comparison, edgeR's *t* tests relative to a threshold ($\text{glmTreat}()$, $\text{lfc} = 1$) method correcting for batch effects was used to identify differentially expressed genes between experimental groups. Genes with a fold change (FC) > 2 and multiple test corrected (FDR) *P* values < 0.05 were selected for further comparisons between treatments and analyzed by Ingenuity Pathway Analysis (IPA) for biological involvement. Additional details regarding RNA-seq analysis are available in the Supplementary Materials.

ChIP and ChIP-seq

Chromatin immunoprecipitation (ChIP)-qPCR and ChIP-sequencing (ChIP-seq) were carried out as before (28). For H3K27me3 and H3K36me3 ChIP-seq, 40 million of cells were cross-linked with 1% formaldehyde for 10 minutes, followed by addition of glycine to stop cross-linking. After washing, cell lysis, and sonication, the chro-

matin samples were incubated with antibody-conjugated Dynabeads (Invitrogen) at 4°C. Beads bound with chromatin were then subject to extensive washing and elution. Eluted chromatin was de-cross-linked overnight at 65°C, followed by protein digestion with proteinase K and DNA purification with Qiagen PCR purification kit. The obtained ChIP DNA samples were submitted to the UNC-Chapel Hill High-Throughput Sequencing Facility for preparation of multiplexed libraries and deep sequencing with an Illumina High-Seq platform according to the manufacturer's instructions. Tag counts between DMSO controls and EZH2i-treated samples were then determined across the entire mouse genome using Bedtools multicov and \log_2 fold change and percent change (i.e., decrease or increase) was calculated (29). To compare DMSO controls with EZH2i-treated samples, DeepTools bamCoverage tool was used to calculate tag coverage for the following mouse genes: *cdkn2a*, *Igf2bp3*, *Dab2ip*, *Gzma*, *Upp1*, *Tgm2*, *Fbxo2*, and *Kit* (30). Additional details regarding ChIP sequencing analysis are available in the Supplementary Materials.

Quantification and statistical analysis

Please refer to the appropriate methods section for proteomics and sequencing data set statistical methods. Otherwise, comparisons for two groups were calculated using unpaired two-tailed Student *t* tests, and comparisons for more than two groups were calculated using one-way ANOVA followed by Bonferroni multiple comparison tests. Comparisons over time were calculated using two-way ANOVA followed by Bonferroni multiple comparison tests. For Kaplan-Meier plots of survival, log-rank test was used to determine *P* values. Data were analyzed using GraphPad Prism 7, R Studio, and Microsoft Excel.

Results

EZH2 inhibition induces T-cell exhaustion and dysfunction

To establish the repression of EZH2 (H3K27me3) during tumor infiltration, we purified TILs from an immune suppressive murine model of melanoma (B16F10; ref. 31). TILs from B16F10 tumors have been demonstrated to be exhausted, and here, we show infiltrating CD4⁺ and CD8⁺ T cells displayed a reduction in H3K27me3 compared with lymphocytes from tumor-draining lymph nodes and *in vitro*-activated T cells (Fig. 1A). To model acute inhibition of EZH2 in activated CD8⁺ T cells, we used highly specific and effective small-molecule inhibitors (EZH2i; Fig. 1B). We believe this approach, in contrast to genetic deletion, more accurately models the loss of T-cell EZH2 activity, which occurs within the tumor environment. Further, this approach also reveals potential unintended consequences affecting T-cell function that could occur with systemic EZH2i anti-cancer therapies. *In vitro* inhibition of EZH2 in primary CD8⁺ T cells leads to a minor effect on their *in vitro* proliferative capacity (Fig. 1C).

RNA-seq and proteomic analysis were performed on *in vitro*-activated cytotoxic T cells (CD8⁺) treated after activation (48 hours) with EZH2i for 48 hours as in Fig. 1B. RNA-seq and proteomic datasets revealed an exhausted phenotype induced by the *in vitro* inhibition of EZH2 (Fig. 1D). A significant increase in inhibitory receptors (Pdc1, Lag3, Tigit) and loss of memory markers (Cxcr3, Cd62L) was consistent at both transcript and protein levels, indicating EZH2i effects negatively control T-cell function. Further, the exhaustion-driving transcription factors Nr4a (Nrfa1, Nrfa2, Nrfa3), Tox, and Tox2 were also elevated in EZH2i-treated CD8⁺ T cells (Fig. 1E). In an *in vitro* setting, EZH2i had no effect on the ability of OT-1⁺ T cells to kill MC38^{SIINFEKL} tumor cells. Target tumor cells were engineered to express the ovalbumin antigen SIINFEKL and were

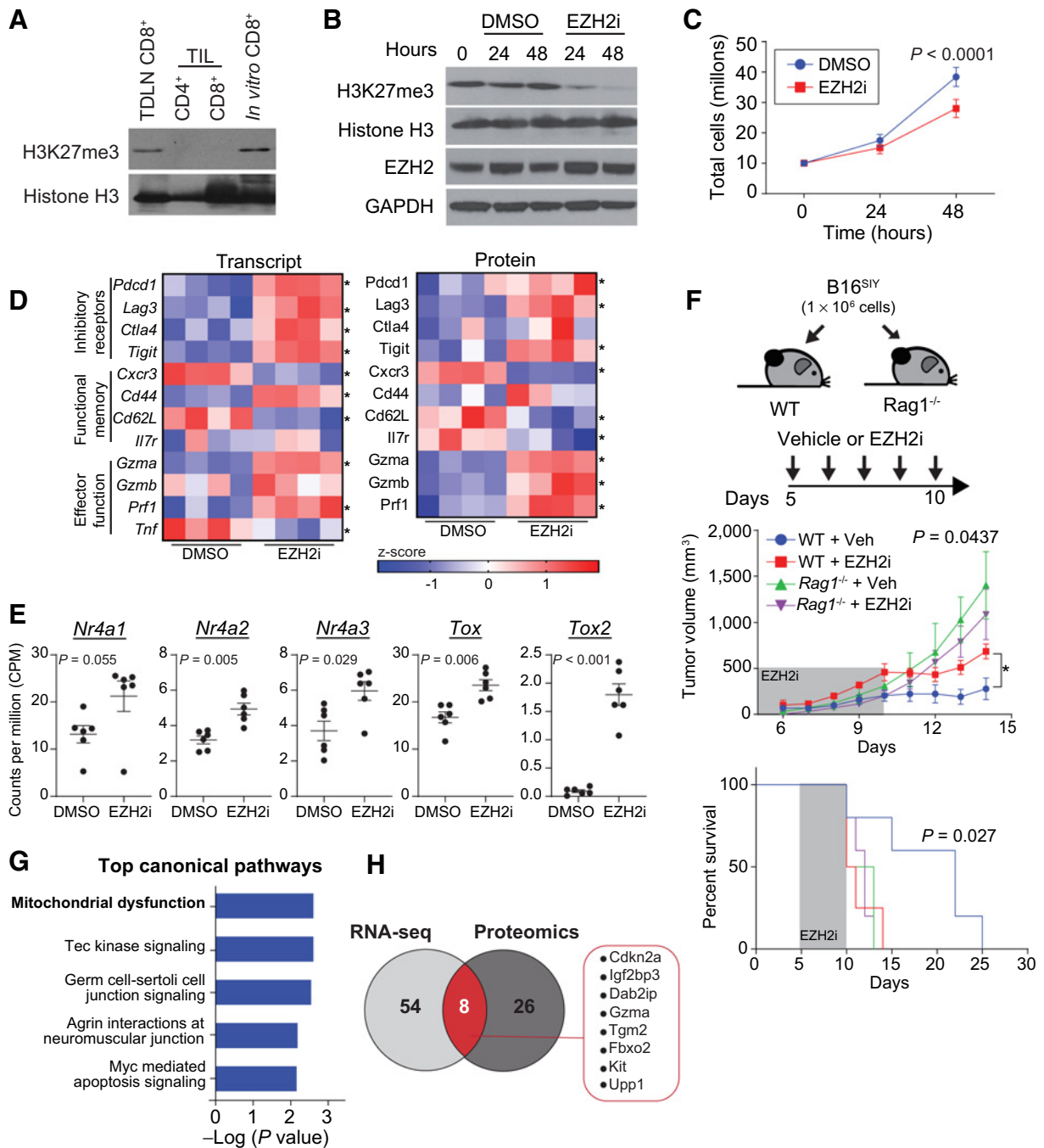


Figure 1.

Systems approach uncovers drivers of T-cell exhaustion resulting from EZH2 inhibition. **A**, Western blot analysis of TDLN and B16F10 melanoma TIL populations. FACS was used to purify CD4⁺ and CD8⁺ lymphocyte populations and *in vitro*-activated (CD3e/CD28) CD8⁺ T cells were used as a positive control. **B**, Western blot analysis of *in vitro* preactivated, primary CD8⁺ T cells treated with EZH2i (EPZ6438, 2.5 μmol/L) for 24 or 48 hours. In all experiments, CD8⁺ T cells were purified prior to activation. **C**, The proliferation of preactivated CD8⁺ T cells ±EZH2i was determined using trypan blue exclusion ($n = 5$). Error bars, SEM. **D**, Subset of genes involved in T-cell effector function and exhaustion from RNA-seq and proteomic analysis of EZH2i-treated preactivated CD8⁺ T cells. The RNA-seq heatmap was generated using logCPM values (Z-score), and asterisks signify an adjusted P value < 0.05 (Holm-Sidak). The protein heatmap was generated from normalized tandem mass tag intensities (Z-score), and asterisks signify an adjusted P value < 0.05 (Holm-Sidak). **E**, Subset of exhaustion associated transcription factors from RNA-seq dataset. **F**, C57BL/6 (immune competent) or Rag1^{-/-} (immune compromised) mice were injected subcutaneously with 1 × 10⁶ B16SIY cells. Starting on day 5, mice were injected (orally) with vehicle (0.5% w/v methyl cellulose and 0.1% Tween-80) or 250 mg/kg EPZ6438 twice daily for 5 consecutive days. Tumor growth curves depict an average tumor volume in each group ($n = 5-6$). Error bars, SEM. Kaplan-Meier survival of recipient mice (tumor size > 500 mm³). P value denotes statistical significance by log-rank test. **G**, Significantly altered gene lists from IPA of proteomic data. **H**, Venn diagram comparing significant genes identified in RNA-seq and proteomics data sets.

validated using Elispot (Supplementary Fig. S1A and S1B). This suggests that EZH2i does not simply lead to a difference in the strength of activation.

In vivo, EZH2 inhibition blocks immune control of the highly immunogenic murine model of melanoma, B16F10^{SIY} (Fig. 1F). B16F10^{SIY} cells are engineered to express the model antigen, SIY (SIYRYGL), and have a well-documented growth delay in immune-competent recipient mice due to strong immune detection (32). B16F10 cells are resistant to EZH2 inhibition and provide an opportunity to assess the effects of EZH2 inhibitors (EZH2i) on T-cell antitumor activity (33). Treatment with EZH2i increased the growth rate of B16F10^{SIY} tumors *in vivo* and decreased survival in WT mice. This was not observed in the immune-compromised, RAG1^{-/-} mice, suggesting a role in the repression of TILs. However, this does not inform us on the extent or the capacity in which T cells require EZH2 for their function.

Multomics approach uncovers mitochondrial dysfunction as a driver of EZH2 inhibition-induced T-cell exhaustion

In addition to the functional markers above, we quantified the relative abundance of 11,006 protein coding transcripts and 9,301 proteins. EZH2i treatment resulted in 62 transcripts differentially expressed (Log2FC > 2.5, *P* value < 0.05; Supplementary Fig. S2A) and 34 protein levels differentially expressed (Log2FC > 1.25, *P* value < 0.05; Supplementary Fig. S2B). As expected, inhibition of the repressive PRC2 complex generated mostly increases in transcript and protein levels, visualized through volcano plots (Supplementary Fig. S2C and S2D). To prioritize upstream candidate genes and pathways contributing to the exhaustion phenotype, we used two approaches. First, IPA of differentially expressed proteins predicted the most significant cellular pathways in EZH2i-treated T cells largely correspond to mitochondrial dysfunction (Fig. 1G). The genes that define this gene set include: *Gzma*, *Mapk12*, *Tgm2*, *mt-Atp6*, *Cdkn2a*, and *Cox6a1*. Interestingly, elevation of Tec kinase signaling was also identified in the analysis and is known for its role in TCR signaling leading to IL2 induction, which can be a sign of overstimulation and exhaustion (34). Our second approach to prioritize candidates was based on the understanding that EZH2 primarily regulates genes at the transcript level, and therefore most upstream candidates are likely different at both the transcript and protein levels. We regarded the genes found in the union of this multomics approach as possible drivers of exhaustion in EZH2i-treated T cells (Fig. 1H). Taken together, these data suggest EZH2i-driven T-cell exhaustion is, at least in part, due to mitochondrial dysfunction.

Loss of EZH2 function leads to metabolic exhaustion in CD8⁺ T cells

T-cell activation leads to rapid and robust metabolic changes essential to support proliferation and function (35). To further understand possible metabolic changes in response to EZH2 inhibition, we measured OCR and ECAR. Metabolic flux analysis of CD8⁺ T cells treated with EZH2i revealed a defect in basal OCR and substantial loss of spare respiratory capacity (OCR_{Max}-OCR_{Basal}), which are key measurements of mitochondrial respiration and oxidative phosphorylation (OxPhos; Fig. 2A). Naïve T cells were used for comparison and to illustrate the drastic loss in oxygen consumption. EZH2 inhibition resulted in an increased dependence on glycolytic metabolism, indicated by the ratio of basal ECAR/OCR (Glycolysis/OxPhos; Fig. 2B). Parallel analysis of cytotoxic (CD8⁺), helper (CD4⁺, CD25⁻), and regulatory (CD4⁺, CD25⁺) T cells reveals a similar loss in OCR (Fig. 2C; Supplementary Fig. S3A). Consistent with mitochondrial

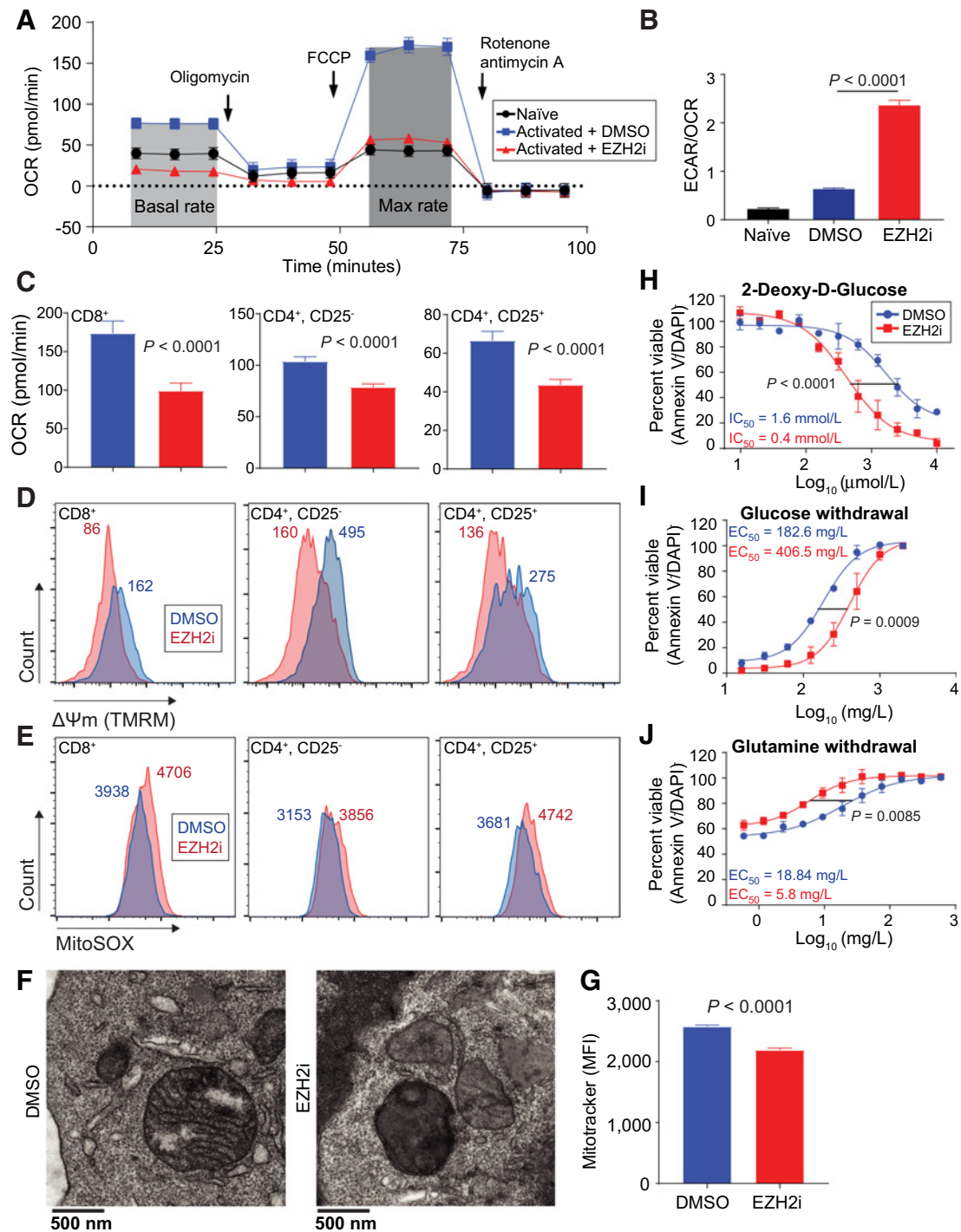
dysfunction, cytotoxic, helper, and regulatory T cells all display a loss of mitochondrial membrane potential (Fig. 2D) and an increase in mitochondrial-derived superoxide species (Fig. 2E) when treated with EZH2i. The metabolic phenotype induced by EZH2 inhibition was replicated in CD8⁺ T cells with an alternative EZH2i, GSK503 (Supplementary Fig. S3C and S3D). Surprisingly, cellular ATP levels were not affected in EZH2i-treated T cells (Supplementary Fig. S3E). This suggests glycolytic metabolism compensates for the loss of mitochondrial respiration and provides the necessary ATP in an *in vitro*, glucose rich environment. Transmission electron microscopy revealed an abnormal mitochondrial morphology in CD8⁺ T cells treated with an EZH2i (Fig. 2F; Supplementary Fig. S3F). We also observed a loss of mitochondrial mass using MitoTracker FM (Fig. 2G).

As the loss of mitochondrial function was clear, we next examined the sensitivity of EZH2-inhibited T cells to metabolic-stress induced cell death. EZH2 inhibition rendered T cells more sensitive to increasing doses of 2-deoxy-D-glucose (glycolysis inhibitor; Fig. 2H) and to the withdrawal of glucose (Fig. 2I). Conversely, EZH2 inhibition reduced the sensitivity to the withdrawal of glutamine, a mitochondrial substrate (Fig. 2J). EZH2 inhibition also leads to a sensitivity of T cells to oxidative stress (H₂O₂; Supplementary Fig. S3G) and pan-kinase inhibition (Staurosporine; Supplementary Fig. S3H). Thus, EZH2 inhibition causes a dramatic shift in T-cell dependency on glycolytic metabolism, rendering them metabolically exhausted and sensitive to further insult including glucose withdrawal.

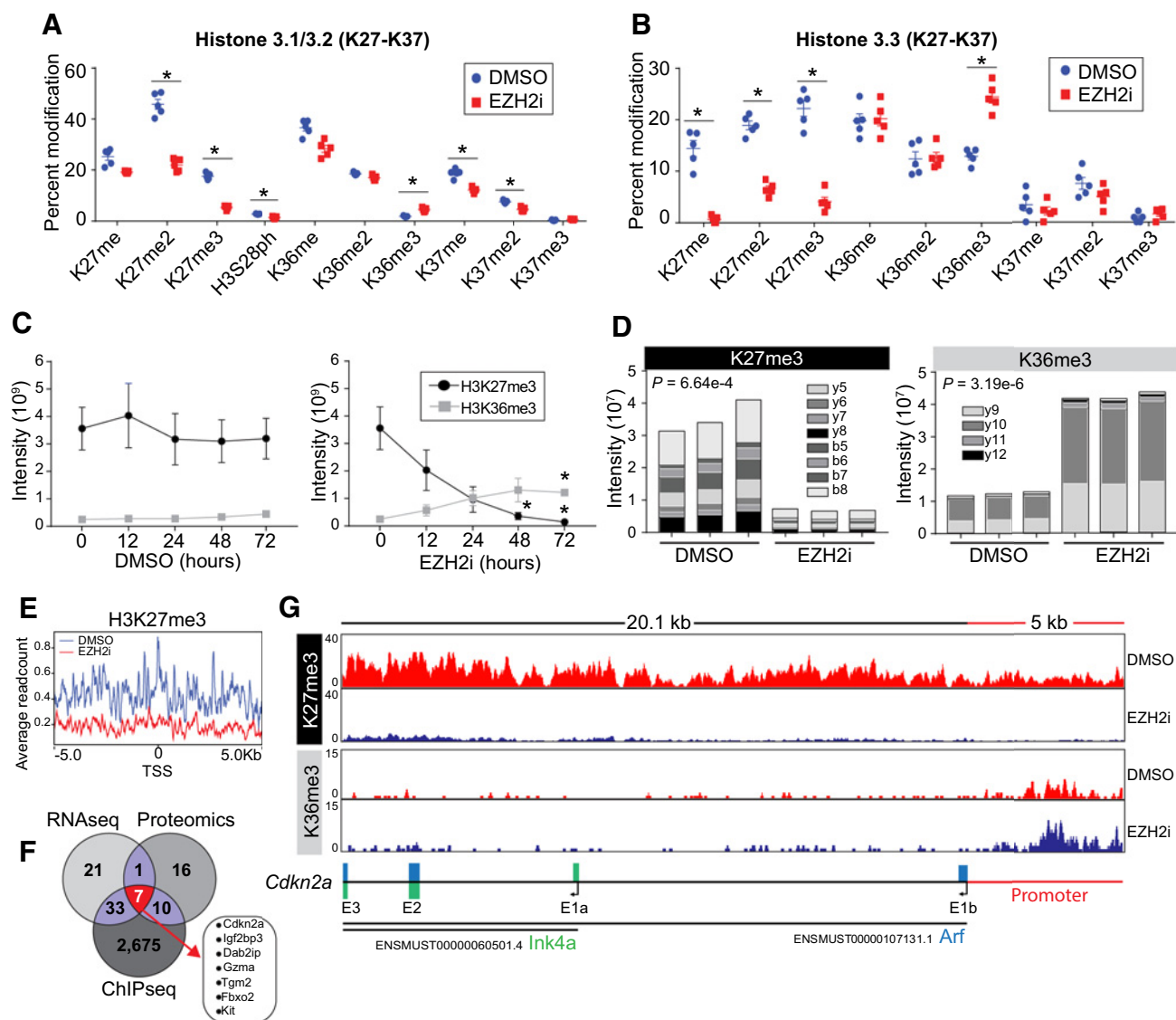
EZH2 inhibition leads to histone epigenetic reprogramming at the Cdkn2a locus

The connection between EZH2 inhibition and mitochondrial dysfunction has not been previously explored. To further prioritize our target genes driving the mitochondrial phenotype, we sought to connect the expression analysis directly to histone epigenetic control. First, to determine the histone PTM landscape after EZH2 inhibition in T cells, we performed a high-resolution mass spectrometric analysis of acid-extracted histones from T cells after EZH2 inhibition (Supplementary Fig. S4A). We quantified the relative abundance of approximately 30 unique histone modifications (monomethylation, dimethylation, trimethylation, phosphorylation, and acetylation) and combinatorial status where possible (Fig. 3A and B; Supplementary Fig. S4B–S4D). Relative spectral counting of PTMs on the functionally distinct histone H3.1 (DNA synthesis) and H3.3 (DNA synthesis independent) revealed a global reduction H3K27me2/3 as expected. We did not detect a large-scale remodeling of the histone landscape, and most of the PTMs detected were not altered between the groups. However, aside from K27me/me2/me3 changes, we detected significant changes in s28ph, k36me3, and k37me/me2 on H3.1. Interestingly, we observed an elevation of H3K36me3 on both H3.1 and H3.3, a histone PTM thought to be involved in gene elongation and alternative splicing (36). Time course analysis revealed that T cells have near undetectable levels of H3K36me3, and this changed as H3K27me2/3 is lost due to EZH2 inhibition (Fig. 3C). The presence of H3K36me3 was confirmed using parallel reaction monitoring (PRM) and targeted mass spectrometry (Fig. 3D; ref. 37). These data indicate that a loss of the repressive mark, H3K27me3, coincides with a certain degree of accumulation of H3K36me3 in EZH2i-treated cells.

In accordance with the histone proteomics, ChIP-sequencing revealed a genome-wide reduction in H3K27me3 level in the EZH2i-treated cells. For instance, in a window of ±5 kb from the transcription start site (TSS), we demonstrated a significant decrease in average read count (ARC) of H3K27me3 (ARC: 0.2), compared with control (0.4; Fig. 3E). Although the EZH2 inhibition does not

**Figure 2.**

Loss of EZH2 leads to metabolic exhaustion in $CD8^+$ T cells. **A**, Representative trace of OCR in preactivated $CD8^+$ T cells treated for 48 hours with EZH2i. Arrows, injection time of respective inhibitors, oligomycin (ATP synthase inhibitor), FCCP (uncoupler), and rotenone + antimycin (complex I and III). Naïve T cells were used for comparison. **B**, Glycolytic dependency determined by the ratio of ECAR and OCR. Data represent the mean, and error bars represent the SEM. P value was determined by unpaired t test. **C-E**, Parallel analysis of activated cytotoxic ($CD8^+$), helper ($CD4^+CD25^-$), and regulatory ($CD4^+CD25^+$) T cells \pm EZH2i. OCR (C), mitochondrial membrane potential (TMRM; D), and mitochondrial superoxide species (MitoSOX; E). Histogram median fluorescent intensity (MFI) is indicated. **F**, Representative transmission electron microscopy of activated $CD8^+$ T cells \pm EZH2i. Data represent the mean ($n = 3$), and error bars represent the SEM. P value was determined by unpaired t test. **H and J**, Viability was determined by Annexin-V/DAPI staining in $CD8^+$ T-cell cultures treated with increasing doses of 2-DG (H), glucose withdrawal (I), and glutamine withdrawal (J) for 24 hours. Data represent the mean ($n = 3$), and error bars represent SEM. Sum-of-squares F test was used for statistical comparison of IC_{50} s.

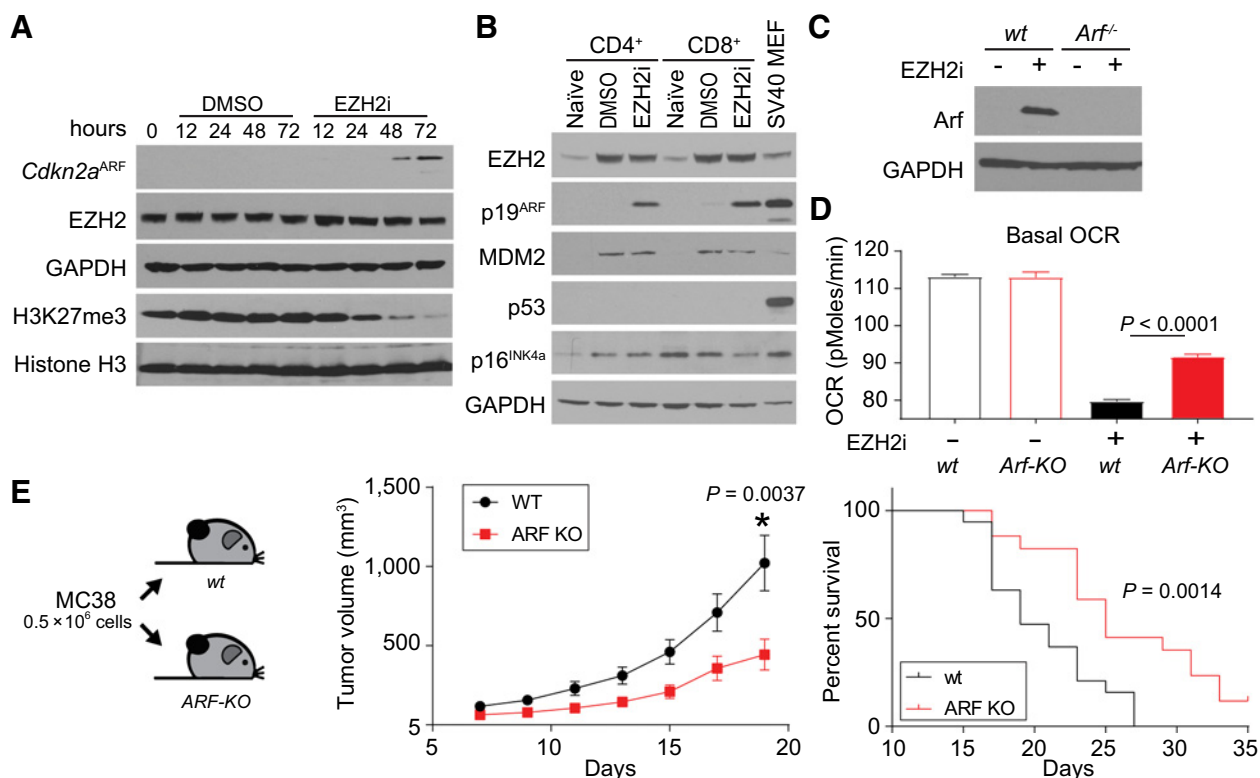
**Figure 3.**

Loss of H3K27me3 leads to histone epigenetic reprogramming at the *Cdkn2a* locus. **A** and **B**, Proteomic analysis of acid-extracted histones from *in vitro*-activated CD8⁺ T cells treated after activation with vehicle or EZH2i. Relative abundance of histone H3.1/2 (**A**) and histone H3.3 (**B**) after translational modifications is presented as a percentage of total peptide spectral counts. Individual replicates ($n = 5$) are plotted as a mean, and error bars represent SEM. Asterisks denote corrected P value < 0.05 (Holm-Sidak). **C**, Proteomic quantification of H3K36me3 and H3K27me3 from time points after EZH2i treatment. Data represent the mean ($n = 3$), and error bars represent SEM. Asterisks signify an adjusted P value < 0.05 (two-way ANOVA). **D**, PRM mass spectrometry for H3K36me3 and H3K27me3 from activated T cells 48 hours after EZH2i inhibition. The specific b and y ion series noted were used to distinguish K36 and K27 trimethylation. Representative data from three biological replicates. **E**, ARCs of H3K27me3 relative to the global TSS ± 5 kb. **F**, H3K27me3 ChIP-seq of control and EZH2i-treated T cells. Note that 2,725 loci with a $\log_2FC > 2.5$ were identified, and a Venn diagram was used to compare genes identified in RNA-seq, proteomics, and ChIP-seq data sets. **G**, IGV views of H3K27me3 and H3K36me3 read densities at the *Cdkn2a* locus. Bottom schematic shows the distribution of *Arf* and *Ink4a* exons.

necessarily affect the occupancy or enrichment of H3K36me3 at the ± 5 kb of global TSS site (Supplementary Fig. S5A), we observed enrichment of H3K36me3 at the body of several differentially over-expressed ($\log_2FC > 2.5$ genes, $N = 18$), including *Tgm2*, *Gzma*, *Dab2ip*, or *Kit* of the most significant candidates from the RNA-seq and proteomic data sets (Fig. 3F). Interestingly, EZH2i induced an elevation of H3K36me3 at the *Cdkn2a* promoter (Fig. 3G). The *Cdkn2a* promoter was previously reported to contain bivalent chromatin marks, overlapped at the hypomethylated CpG Island. Induced

demethylation resulted in complete loss of H3K27me3 at the gene promoter, leading to a gain in H3K27ac (38). Herein, we observed that induced removal of H3K27me3 is concomitant with accumulation of H3K36me3 at the promoter. Increment in gene expression ($\log_2FC = 4.36$) hence can be reasonably correlated to the switch in occupancy from H3K27me3 to the activating H3K36me3, H3K27ac, etc. marks at the *Cdkn2a* promoter in the EZH2i-inhibited cells.

The shift in epigenetic regulation at the *Ink4a-Arf* (*Cdkn2a*) locus and release of this gene had significant downstream effects, as

**Figure 4.**

Arf induces metabolic exhaustion independent of p53. **A** and **B**, Representative Western blot analysis of candidate protein Arf in an EZH2 inhibitor time course (**A**) and both preactivated CD4⁺ and CD8⁺ T cells (**B**). SV40-transformed mouse embryonic fibroblasts (MEF) were used as a positive control. **C**, Representative Western blot analysis of EZH2i-treated wt and Arf^{-/-} CD8⁺ T cells. **D**, OCR in activated CD8⁺ wt or Arf-KO-activated T cells treated for 48 hours ±EZH2i. *P* value was determined by unpaired *t* test. **E**, C57Bl/6 wt or Arf-KO mice were challenged with MC38 tumor cells. Tumor growth curves depict an average tumor volume in each group (*n* = 15–20). Error bars, SEM. Kaplan–Meier survival of recipient mice (tumor size > 1,000 mm³). *P* value denotes statistical significance by log-rank test.

evidenced by the gene products presenting as top hits in RNA-seq and proteomic data sets. *Cdkn2a* encodes two tumor suppressors, Ink4a and Arf, which are not expressed in most normal tissues (39). Arf (p19^{Arf}) is derived from *Cdkn2a* through an alternative reading frame product (*Arf*). Prior studies have revealed Arf exerts potent antiproliferative effects and *Cdkn2a* is known to be repressed by H3K27me3 in cancer cells (40). Background evidence for *Cdkn2a* regulating cellular responses to stress, along with the high fidelity of this gene through multiomics analysis, implored selection for mechanistic follow-up studies. Peptide mapping confirmed Arf as the protein dysregulated at this locus (Supplementary Fig. S6A). In addition, Arf expression was validated by a series of Western blot analysis experiments: time course of EZH2 inhibition (Fig. 4A), both CD4⁺ and CD8⁺ T cells (Fig. 4B), and using an alternative EZH2 inhibitor, CPI-1205 (Supplementary Fig. S6B). Collectively, our genome-wide profiling further implicates epigenetic remodeling of the *Cdkn2a* locus as an event in EZH2 inhibition-induced T-cell exhaustion.

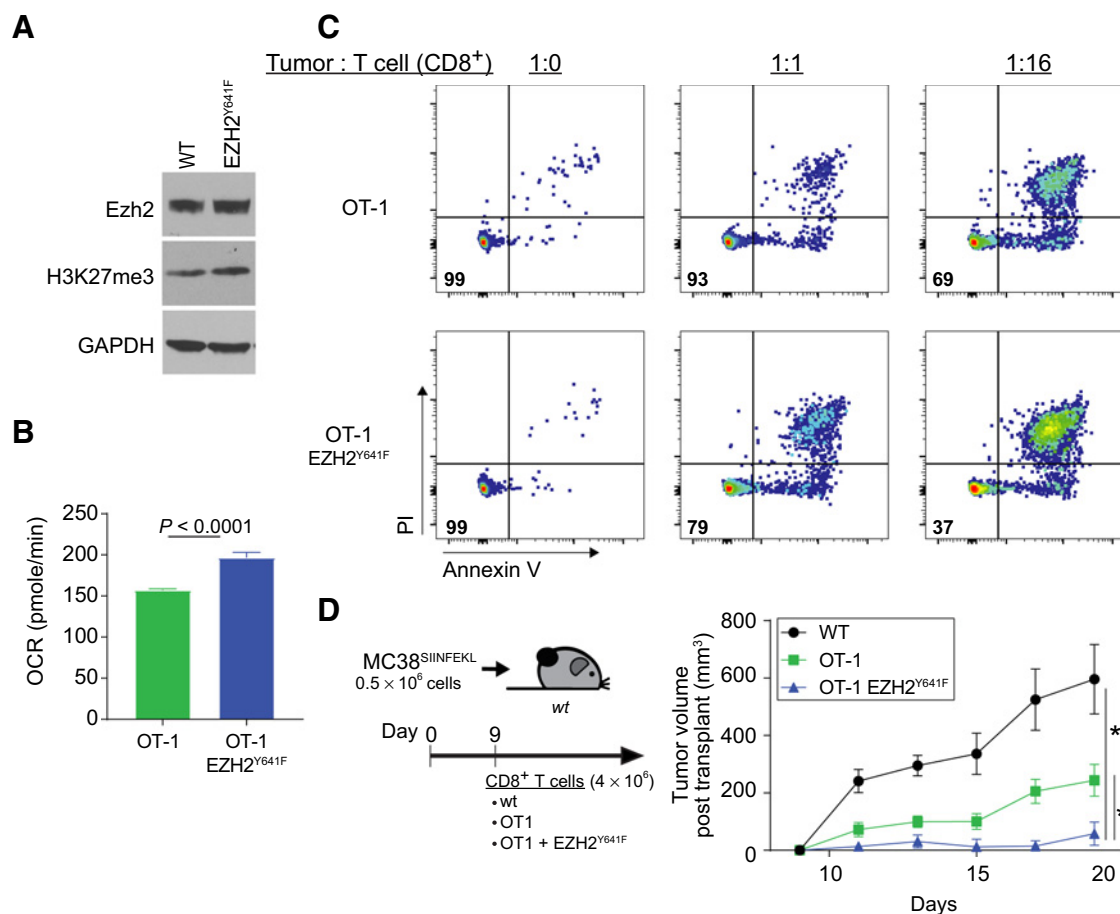
Arf induces metabolic exhaustion independent of p53

Arf is well known to exert tumor-suppressor activity through inhibition of MDM2, stabilizing p53, which leads to robust cell-cycle arrest and cell death (41, 42). Surprisingly, in this case, Arf had minor effects on T-cell survival and cell-cycle progression (Supplementary Fig. S6C). Consistent with this finding, in both CD4⁺ and CD8⁺ lymphocytes, we did not detect a stabilization of p53 upon EZH2-inhibition (Fig. 4B). One of the hallmarks of p53 stabilization is

the effect on the intrinsic apoptotic machinery (BCL-2 family). For example, p53 is well known to induce the expression of the proapoptotic PUMA, which we did not observe (Supplementary Fig. S6D and S6E). Also, there was no detectable cleavage of the caspase target, PARP (Supplementary Fig. S6E). Interestingly, the transcript levels of p53 dropped in response to EZH2 inhibition (Supplementary Fig. S6F). These data suggest Arf acts independently of p53 in these cells.

It is an intriguing possibility that epigenetic control of Arf directly contributes T-cell metabolic exhaustion. Arf has been reported to interact with the mitochondrial protein p32/C1QBP, which was shown to lead to mitochondrial damage (43). In addition, there is an N-terminally truncated Arf protein (smARF) that lacks the residues required for p53 activation and has been reported to localize to mitochondria and trigger mitophagy (44, 45). To directly assess the contribution of Arf expression to T mitochondrial dysfunction, we utilized an Arf knock out (Arf-KO) mouse model, which only disrupts Arf expression at the *Cdkn2a* locus (Fig. 4C; ref. 39). Arf deficiency was able to partially restore the loss of OCR induced by EZH2 inhibition in T cells (Fig. 4D). ARF plays a role in driving T-cell metabolic dysfunction in the tumor environment, though this datum suggests that there are additional or compensatory mechanisms at play.

Our data suggest that EZH2 acts as a critical mediator for mitochondrial sufficiency in part through regulation of the *Arf* locus. To demonstrate the involvement of ARF signaling in T-cell dysfunction, we challenged Arf-deficient (Arf-KO) mice with a murine model colon

**Figure 5.**

Exogenous expression of $EZH2^{Y641F}$ in lymphocytes improves tumor killing and adoptive T-cell therapy. **A**, Western blot analysis of *in vitro*-activated $CD8^+$ wt and Lck- $EZH2^{Y641F}$ T cells. **B**, OCR of preactivated $CD8^+$ wt and Lck- $EZH2^{Y641F}$ T cells. *P* value was determined by unpaired *t* test. **C**, *In vitro* killing assay was used to determine cytotoxic function. Target cells ($MC38^{SINFEKL}$) were cultured with CellTrace-Violet labeled, preactivated OT-1 or OT-1- $EZH2^{Y641F}$ $CD8^+$ T cells at a target/effector ratio of 1:0, 1:1, or 1:16. Tumor killing is presented as the percentage of viable (Annexin V^- , PI $^-$) tumor cells remaining after 10 hours of coculture. Data are representative of two independent experiments. **D**, C57BL/6 mice were inoculated with 5×10^6 $MC38^{SINFEKL}$. After 9 days, 4×10^6 WT, OT-1, or OT-1, $EZH2^{Y641F}$ preactivated $CD8^+$ T cells were transferred *i.v.* into recipients, and tumor growth was assessed. Tumor growth curves depict an average tumor volume in each group ($n = 8-10$). Error bars, SEM. Asterisk denotes statistical significance ($P < 0.01$).

adenocarcinoma (MC38; Fig. 4E). Constitutive deletion of *Arf* leads to an enhanced ability to control tumor growth and significantly increased median survival. However, this did not amount to complete protection and is consistent with the partial rescue of the metabolic phenotype.

Exogenous expression of $EZH2^{Y641F}$ improves tumor control

Approaches to enhance the survivability and metabolic sufficiency of tumor-specific T cells will be important for advancing this approach (46). We assessed whether reprogramming T cells with the gain-of-function $EZH2^{Y641F}$ mutant would enhance their ability to control tumor growth in an ACI mouse model. The $EZH2^{Y641F}$ mutation causes a gain of function of EZH2 by altering its substrate specificity. This mutation increases its activity toward the dimethylated substrate and in concert with a WT allele, causing an increase in the trimethylation of H3K27 (Fig. 5A; ref. 47). Tumor-specific T cells were generated from OT-1 and OT-1-Lck- $EZH2^{Y641F}$ mice. Activated $CD8^+$ T cells expressing the $EZH2^{Y641F}$ mutant had slightly elevated rates of oxygen consumption (Fig. 5B) and were superior at killing of

$MC38^{SINFEKL}$ tumor cells *in vitro* (Fig. 5C). In a model ACI, tumor ($MC38^{SINFEKL}$) bearing mice that received $EZH2^{Y641F}$ -positive OT-1 T cells were able to control tumor growth significantly better than mice that received either tumor-specific (OT-1) and nonspecific (wt) control cells (Fig. 5D). To determine if $EZH2^{Y641F}$ expression simply enhanced the survival of peripheral T cells *in vivo*, we adoptively transferred control and $EZH2^{Y641F}$ -positive T cells into congenic, $CD45.1^+$ recipient mice and tracked donor ($CD45.2^+$) survival (Supplementary Fig. S7A). We found no significant difference in $EZH2^{Y641F}$ T cells within the spleen, lymph nodes, or peripheral blood 2 days after transfer. These findings are consistent with the idea that EZH2 plays a role in the protection of TILs from metabolic stress-induced dysfunction and that manipulation of EZH2 in ACI therapies would be beneficial.

Discussion

Understanding the mechanisms T cells use for protecting metabolic circuits may lead to new strategies and improve the efficacy of cancer

immunotherapies. Engineering adoptive T cells, unconstrained by tolerance-based metabolic circuits, may allow for further advancement of cellular therapies against solid tumors. There have been some successes in overcoming inhibitory tumor metabolism, largely through enforcing mitochondrial respiration (7, 13). For example, the exogenous expression of the transcription factor *Pgc1a*, which directly controls mitochondrial biogenesis and effectively changes the metabolic circuit. However, recent discoveries have highlighted dynamic metabolic processes as drivers of T-cell function. This suggests that genetically or pharmacologically influencing T-cell metabolism will negate their ability to dynamically adapt. The goal therefore is to generate T cells that can withstand metabolic stresses, allowing for metabolic plasticity.

The ability of T cells to generate diverse phenotypes is in part due to histone modifications during the extensive chromatin remodeling occurring upon activation (48). Genetic deletion studies have recently implicated EZH2 (H3K27me3) in the control T-cell effector function and memory precursor formation (49, 50). However, this approach does not simulate an acute loss of EZH2, which TILs undergo during infiltration. In addition, genetic deletion of EZH2 can be compensated for by EZH1 (51). Perhaps more importantly, EZH2i therapies are actively being considered for treatment of a variety of advanced solid tumors (e.g., NCT02601950, NCT03213665) and in some cases in combination with immune checkpoint inhibition (NCT03525795). These studies are motivated by a recently realized toxicity to T regulatory cells and the ability of H3K27me3 to mediate Th1-type chemokine expression in tumor cells (20, 52). However, our work sheds light on the deleterious effects of EZH2 inhibition on other T-cell subsets and suggests the use of these drugs in combination with immunotherapy may be challenging.

In the present study, we report the identification of EZH2 (H3K27me3) as a protector of T-cell metabolic sufficiency. Through a systematic evaluation of H3K27me3 loss, which occurs during tumor infiltration, we have discovered an epigenetic mechanism that contributes to the development of tumor-induced metabolic exhaustion in T cells. Loss of PRC2-repressive activity, through acute inhibition of EZH2, leads to a metabolic insufficiency in T cells. This has been characterized by the loss of mitochondrial respiration, loss of mitochondrial membrane potential, and increased sensitivity to glucose withdrawal. Our data emphasize the coordination of histone epigenetics and T-cell metabolic exhaustion. These findings are consistent with recent work defining a role for EZH2 in metabolic reprogramming of cancer cells (53, 54).

We identified the EZH2 inhibition-induced mitochondrial dysfunction phenotype using cutting-edge proteomics and gene set enrichment analysis. Using metabolic flux analysis to measure OCR (mitochondrial respiration) and acidification rates (glycolysis), we validated the loss of mitochondrial sufficiency in both CD4⁺ and CD8⁺ T cells using multiple specific inhibitors of EZH2. The elevated glycolytic rates induced by EZH2 inhibition are consistent with mitochondrial damage and indicate a strong glycolytic dependence. This metabolic phenotype is consistent with metabolic exhaustion in TILs, which is thought to be a driving force of functional exhaustion (55). To mimic the glucose withdrawal present in solid tumors, we treated with 2-Deoxy-D-Glucose (glycolysis inhibitor) or altered the concentration of glucose. EZH2 inhibition sensitized T cells to these metabolic stresses, a process that we believe occurs during tumor infiltration.

The ability of EZH2 to protect mitochondrial integrity has not been previously explored. Our comparison of proteomics, RNA-seq,

and ChIP-sequencing approaches greatly narrowed down the H3K27me3-controlled candidate genes involved in driving mitochondrial dysfunction. Surprisingly, we did not find that EZH2 was directly regulating any conical metabolic pathways (fatty acid metabolism, glucose metabolism, electron transport, etc.). However, *Cdkn2a^{Arf}* was a top candidate in all these approaches and known to be repressed by EZH2 (H3K27me3) in cancer cells (56). The regulation of the *Cdkn2a* locus has been previously described in EZH2-KO T cells and was associated with prolonged division times, leading to a minor reduction in proliferation (57). This is likely due to the fact that in activated T cells, the expression of *Arf* does not lead to the canonical stabilization of p53, which is necessary for downstream cell-cycle arrest or cell death due to a strong repression of the *Trp53* through engagement of TCR signaling (58). This observation leads us to propose alternative p53-independent mechanisms. We show that genetic deletion of *Arf* can rescue the metabolic defect induced during EZH2 inhibition. Thus, we propose that *Arf* induces mitochondrial dysfunction and therefore the downstream metabolic exhaustion. This p53-independent mechanism has been proposed and is thought to work through an interaction with the mitochondrial protein p32/C1QBP (43). p32 is predominantly localized to the mitochondria where it has a functional role in maintaining oxidative phosphorylation (59, 60). Furthermore, we show that *Arf*^{-/-} animals have better control of colon adenocarcinoma (MC38) growth.

Therapeutically, this study suggests that enhancing/protecting EZH2 in cytotoxic T cells would be beneficial. One of the most common mutations of EZH2 in cancer cells is Y641F, a gain-of-function mutation that elevates H3K27me3 (61). We engineered tumor-specific T cells to express the EZH2^{Y641F} mutation, and it did, in fact, enhance the ability to control tumor growth *in vitro* and in adoptive T-cell transplant experiments. Additional studies will be necessary to fully explore the potential of utilizing EZH2 gain-of-function mutants in cellular transplant studies.

Limitations

As outlined above, our results demonstrate that EZH2 through the placement of H3K27me3 contributes to the protection of mitochondrial sufficiency within T cells. However, we did not explore potential nonenzymatic roles for EZH2, which have been proposed to be an important aspect of EZH2 biology (62). Understanding the full scope of EZH2 in T-cell biology is challenging, especially when paired with conflicting roles of EZH2 within the context of tumor immunology and anticancer therapies. There are many important facets to T cells, and EZH2 exerts broad regulatory control through modifying the epigenome. Although *Arf* was clearly a top candidate gene in our studies, we did identify other potentially important candidates including *Gzma*, which has also been implicated in mitochondrial dysfunction (63). Nevertheless, our findings provide an innovative perspective on the control of metabolic exhaustion of T cells during tumor infiltration and provide rationale for the clinical development of gain-of-function EZH2 T-cell therapies.

Disclosure of Potential Conflicts of Interest

T.C. Chiang reports grants and personal fees from National Cancer Research during the conduct of the study. T.F. Gajewski reports grants and personal fees from Merck, grants from BMS, grants and personal fees from Aduro, grants and personal fees from Evelo, grants and personal fees from Pyxis, personal fees from Jounce, personal fees from FogPharma, personal fees from Adaptimmune, and personal fees from Allogene outside the submitted work. No potential conflicts of interest were disclosed by the other authors.

Authors' Contributions

B. Koss: Conceptualization, resources, data curation, formal analysis, funding acquisition, validation, investigation, visualization, methodology, writing-original draft, writing-review and editing. **B.D. Shields:** Validation, investigation, writing-original draft, writing-review and editing. **E.M. Taylor:** Validation, investigation. **A.J. Storey:** Data curation, software, formal analysis, methodology. **S.D. Byrum:** Software, formal analysis, methodology. **A.J. Gies:** Software, formal analysis, methodology. **C.L. Washam:** Software, formal analysis, methodology. **S. Roy Choudhury:** Formal analysis, methodology, writing-original draft. **J. Hyun Ahn:** Data curation, methodology. **H. Uryu:** Data curation, methodology. **J.B. Williams:** Resources, investigation, methodology. **K.J. Krager:** Investigation, methodology. **T.-C. Chiang:** Data curation, methodology. **S.G. Mackintosh:** Resources, data curation, methodology. **R.D. Edmondson:** Resources, data curation, methodology. **N. Aykin-Burns:** Resources. **T.F. Gajewski:** Resources, supervision. **G.G. Wang:** Resources, supervision. **A.J. Tackett:** Conceptualization, resources, supervision, funding acquisition, project administration, writing-review and editing.

Acknowledgments

The authors would like to thank the UAMS Biochemistry Department, members of the Tackett laboratory, and Drs. J. Opferman, M. Cannon, S. Taverna, K. Raney, T. Chambers, and C. O'Brien for their helpful discussion. The authors would also like to thank the UAMS Division of Laboratory Animal Medicine, the UAMS Genetic Models Core, the UAMS Proteomics Core, the UAMS Flow Cytometry Core, and the Arkansas Children's Research Institute Bioinformatics Core.

We acknowledge support from NIH grants F31CA232464 (B. Koss), P20GM121293 (A.J. Tackett), and R01CA236209 (A.J. Tackett) and the Scharlau Family Endowed Chair in Cancer Research to A.J. Tackett. This study was additionally supported by the NIH P20GM109005 (N. Aykin-Burns).

The costs of publication of this article were defrayed in part by the payment of page charges. This article must therefore be hereby marked *advertisement* in accordance with 18 U.S.C. Section 1734 solely to indicate this fact.

Received February 13, 2020; revised June 4, 2020; accepted August 28, 2020; published first October 1, 2020.

References

- O'Donnell JS, Teng MWL, Smyth MJ. Cancer immunoediting and resistance to T cell-based immunotherapy. *Nat Rev Clin Oncol* 2019;16:151–67.
- Jiang Y, Li Y, Zhu B. T-cell exhaustion in the tumor microenvironment. *Cell Death Dis* 2015;6:e1792.
- Blank CU, Haanen JB, Ribas A, Schumacher TN. The "cancer immunogram" *Science* 2016;352:658–60.
- Odorizzi PM, Pauken KE, Paley MA, Sharpe A, Wherry EJ. Genetic absence of PD-1 promotes accumulation of terminally differentiated exhausted CD8+ T cells. *J Exp Med* 2015;212:1125–37.
- McKinney EF, Smith KGC. Metabolic exhaustion in infection, cancer and autoimmunity. *Nat Immunol* 2018;19:213–21.
- Buck MD, Sowell RT, Kaech SM, Pearce EL. Metabolic instruction of immunity. *Cell* 2017;169:570–86.
- Buck MD, O'Sullivan D, Klein RI, Huber TB, Rambold AS, Pearce EL. Mitochondrial dynamics controls T cell fate through metabolic programming correspondence. *Cell* 2016;166:63–76.
- Zhang L, Romero P. Metabolic control of CD8+ T cell fate decisions and antitumor immunity. *Trends Mol Med* 2018;24:30–48.
- Wei J, Raynor J, Nguyen TLM, Chi H. Nutrient and metabolic sensing in T cell responses. *Front Immunol* 2017;8:247. DOI:10.3389/fimmu.2017.00247.
- Sukumar M, Roychoudhuri R, Restifo NP. Nutrient competition: a new axis of tumor immunosuppression. *Cell* 2015;162:1206–8.
- Medina G, Vera-Lastra O, Peralta-Amaro AL, Jiménez-Arellano MP, Saavedra MA, Cruz-Domínguez MP, et al. Metabolic syndrome, autoimmunity and rheumatic diseases. *Pharmacol Res* 2018;133:277–88.
- Delgoffe GM, Powell JD. Feeding an army: the metabolism of T cells in activation, anergy, and exhaustion. *Mol Immunol* 2015;68:492–6.
- Scharping NE, Menk AV, Moreci RS, Whetstone RD, Dadey RE, Watkins SC, et al. The tumor microenvironment represses T cell mitochondrial biogenesis to drive intratumoral T cell metabolic insufficiency and dysfunction. *Immunity* 2016;45:701–3.
- Kishton RJ, Sukumar M, Restifo NP. Cell metabolism review metabolic regulation of T cell longevity and function in tumor immunotherapy. *Cell Metab* 2017;26:94–109.
- Le Bourgeois T, Strauss L, Aksoylar HI, Daneshmandi S, Seth P, Patsoukis N, et al. Targeting T cell metabolism for improvement of cancer immunotherapy. *Front Oncol* 2018;8:237.
- Phan AT, Goldrath AW, Glass CK. Metabolic and epigenetic coordination of T cell and macrophage immunity. *Immunity* 2017;46:714–29.
- Zhao E, Maj T, Kryczek I, Li W, Wu K, Zhao L, et al. Cancer mediates effector T cell dysfunction by targeting microRNAs and EZH2 via glycolysis restriction. *Nat Immunol* 2015;17:95–103.
- Laugesen A, Højfeldt JW, Helin K. Molecular cell review molecular mechanisms directing PRC2 recruitment and H3K27 methylation. *Mol Cell* 2019;74:8–18.
- Emran AAI, Chatterjee A, Rodger EJ, Tiffen JC, Gallagher SJ, Eccles MR, et al. Targeting DNA methylation and EZH2 activity to overcome melanoma resistance to immunotherapy. *Trends Immunol* 2019;40:328–44.
- Goswami S, Apostolou I, Zhang J, Skepner J, Anandhan S, Zhang X, et al. Modulation of EZH2 expression in T cells improves efficacy of anti-CTLA-4 therapy. *J Clin Invest* 2018;128:3813–18.
- He S, Liu Y, Meng L, Sun H, Wang Y, Ji Y, et al. Ezh2 phosphorylation state determines its capacity to maintain CD8+ T memory precursors for antitumor immunity. *Nat Commun* 2017;8:2125.
- Karantanos T, Chistofides A, Barhdan K, Li L, Boussiotis VA. Regulation of T cell differentiation and function by EZH2. *Front Immunol* 2016;7:172.
- Hackstadt T, Scidmore MA, Rockey DD. Lipid metabolism in Chlamydia trachomatis-infected cells: directed trafficking of Golgi-derived sphingolipids to the chlamydial inclusion. *Proc Natl Acad Sci U S A* 1995;92:4877–81.
- Huang SK, Scruggs AM, Donaghy J, Horowitz JC, Zaslon Z, Przybranowski S, et al. Histone modifications are responsible for decreased Fas expression and apoptosis resistance in fibrotic lung fibroblasts. *Cell Death Dis* 2013;4:e621.
- Wis' niewski JR, Zougman A, Nagaraj N, Mann M. Universal sample preparation method for proteome analysis. *Nat Methods* 2009;6:359–62.
- Nesvizhskii AI, Keller A, Kolker E, Aebersold R. A statistical model for identifying proteins by tandem mass spectrometry. *Anal Chem* 2003;75:4646–58.
- Chiang T, Koss B, Su LJ, Washam CL, Byrum SD, Storey A, et al. Effect of sulforaphane and 5-Aza-2'-deoxycytidine on melanoma cell growth. *Medicines* 2019;6:71.
- Cai L, Rothbart SB, Lu R, Xu B, Chen WY, Tripathy A, et al. An H3K36 methylation-engaging tudor motif of polycomb-like proteins mediates PRC2 complex targeting. *Mol Cell* 2013;49:571–82.
- Quinlan AR. BEDTools: the Swiss-army tool for genome feature analysis. *Curr Protoc Bioinformatics* 2014;47:11.12.1–34.
- Ramírez F, Dündar F, Diehl S, Grüning BA, Manke T. DeepTools: a flexible platform for exploring deep-sequencing data. *Nucleic Acids Res* 2014;42:W187–91.
- Leclerc M, Voilin E, Gros G, Corgnac S, De Montpréville V, Validire P, et al. Regulation of antitumor CD8 T-cell immunity and checkpoint blockade immunotherapy by Neuropilin-1. *Nat Commun* 2019;10:3345.
- Kline J, Brown IE, Zha Y-Y, Blank C, Strickler J, Wouters H, et al. Homeostatic proliferation plus regulatory T-cell depletion promotes potent rejection of B16 melanoma. *Clin Cancer Res* 2008;14:3156–67.
- Zingg D, Arenas-Ramírez N, Sahin D, Haeusel J, Sommer L, Boyman O, et al. The histone methyltransferase Ezh2 controls mechanisms of adaptive resistance to tumor immunotherapy. *Cell Rep* 2017;20:854–67.
- Ferris RL, Lu B, Kane LP. Too much of a good thing? Tim-3 and TCR signaling in T cell exhaustion. *J Immunol* 2014;193:1525–30.
- Michalek RD, Rathmell JC. The metabolic life and times of a T-cell. *Immunol Rev* 2010;236:190–202.
- Li J, Ahn JH, Wang GG. Understanding histone H3 lysine 36 methylation and its deregulation in disease. *Cellular Mol Life Sci* 2019;76:2899–916.
- Sowers JL, Mirfatah B, Xu P, Tang H, Park IY, Walker C, et al. Quantification of histone modifications by parallel-reaction monitoring: a method validation. *Anal Chem* 2015;87:10006–14.

38. King AD, Huang K, Rubbi L, Liu S, Wang CY, Wang Y, et al. Reversible regulation of promoter and enhancer histone landscape by DNA methylation in mouse embryonic stem cells. *Cell Rep* 2016;17:289–302.
39. Kamijo T, Zindy F, Roussel MF, Quelle DE, Downing JR, Ashmun RA, et al. Tumor suppression at the mouse INK4a locus mediated by the alternative reading frame product p19(ARF). *Cell* 1997;91:649–59.
40. Gil J, Peters G. Regulation of the INK4b–ARF–INK4a tumour suppressor locus: all for one or one for all. *Nat Rev Mol Cell Biol* 2006;7:667–77.
41. Kamijo T, Weber JD, Zambetti G, Zindy F, Roussel MF, Sherr CJ. Functional and physical interactions of the ARF tumor suppressor with p53 and Mdm2. *Proc Natl Acad Sci U S A* 1998;95:8292–7.
42. Zhang Y, Xiong Y, Yarbrough WG. ARF promotes MDM2 degradation and stabilizes p53: ARF–INK4a locus deletion impairs both the Rb and p53 tumor suppression pathways. *Cell* 1998;92:725–34.
43. Itahana K, Zhang Y. Mitochondrial p32 is a critical mediator of ARF-induced apoptosis. *Cancer Cell* 2008;13:542–53.
44. Grenier K, Kontogianna M, Fon EA. Short mitochondrial ARF triggers Parkin/PINK1-dependent mitophagy. *J Biol Chem* 2014;289:29519–30.
45. Van Oosterwijk JG, Li C, Yang X, Opferman JT, Sherr CJ, Prives C. Small mitochondrial Arf (smArf) protein corrects p53-independent developmental defects of Arf tumor suppressor-deficient mice. *Proc Natl Acad Sci U S A* 2017;114:7420–5.
46. Xu X, Gnanaprakasam JNR, Sherman J, Wang R. A metabolism toolbox for CAR T therapy. *Front Oncol* 2019;9:322. DOI:10.3389/fonc.2019.00322.
47. Berg T, Thoene S, Yap D, Wee T, Schoeler N, Rosten P, et al. A transgenic mouse model demonstrating the oncogenic role of mutations in the polycomb-group gene EZH2 in lymphomagenesis. *Blood* 2014;123:3914–24.
48. Roh TY, Cuddapah S, Cui K, Zhao K. The genomic landscape of histone modifications in human T cells. *Proc Natl Acad Sci U S A* 2006;103:15782–7.
49. Dobenecker M-W, Park JS, Marcello J, McCabe MT, Gregory R, Knight SD, et al. Signaling function of PRC2 is essential for TCR-driven T cell responses. *J Exp Med* 2018;215:1101–13.
50. Gray SM, Amezcua RA, Guan T, Kleinstein SH, Kaech SM. Polycomb repressive complex 2-mediated chromatin repression guides effector CD8 + T cell terminal differentiation and loss of multipotency. *Immunity* 2017;46:596–608.
51. Wassef M, Luscan A, Aflaki S, Zielinski D, Jansen PWTC, Baymaz HI, et al. EZH1/2 function mostly within canonical PRC2 and exhibit proliferation-dependent redundancy that shapes mutational signatures in cancer. *Proc Natl Acad Sci U S A* 2019;116:6075–80.
52. Nagarsheth N, Peng D, Kryczek I, Wu K, Li W, Zhao E, et al. PRC2 epigenetically silences Th1-type chemokines to suppress effector T-cell trafficking in colon cancer. *Cancer Res* 2016;76:275–82.
53. Pang B, Zheng XR, Tian J-X, Gao T-H, Gu G-Y, Zhang R, et al. EZH2 promotes metabolic reprogramming in glioblastomas through epigenetic repression of EAF2-HIF1 α signaling. *Oncotarget* 2016;7:45134–43.
54. Vantaku V, Putluri V, Bader DA, Maity S, Ma J, Arnold JM, et al. Epigenetic loss of AOX1 expression via EZH2 leads to metabolic deregulations and promotes bladder cancer progression. *Oncogene* 2020;39:6265–85.
55. Bengsch B, Johnson AL, Kurachi M, Odorizzi PM, Pauken KE, Attanasio J, et al. Bioenergetic Insufficiencies due to metabolic alterations regulated by the inhibitory receptor PD-1 are an early driver of CD8+ T cell exhaustion. *Immunity* 2016;45:358–73.
56. Ito T, Teo YV, Evans SA, Neretti N, Sedivy Correspondence JM. Regulation of cellular senescence by polycomb chromatin modifiers through distinct DNA damage- and histone methylation-dependent pathways. *Cell Rep* 2018;22:3480–92.
57. Chen G, Subedi K, Chakraborty S, Sharov A, Lu J, Kim J, et al. Ezh2 regulates activation-induced CD8+ T cell cycle progression via repressing Cdkn2a and Cdkn1c expression. *Front Immunol* 2018;9:549.
58. Watanabe M, Moon KD, Vacchio MS, Hathcock KS, Hodes RJ. Downmodulation of tumor suppressor p53 by T cell receptor signaling is critical for antigen-specific CD4+ T cell responses. *Immunity* 2014;40:681–91.
59. Gotoh K, Morisaki T, Setoyama D, Sasaki K, Yagi M, Igami K, et al. Mitochondrial p32/C1qbp is a critical regulator of dendritic cell metabolism and maturation. *Cell Rep* 2018;25:1800–15.
60. Jiang J, Zhang Y, Krainer AR, Xu RM. Crystal structure of human p32, a doughnut-shaped acidic mitochondrial matrix protein. *Proc Natl Acad Sci U S A* 1999;96:3572–7.
61. Wigle TJ, Knutson SK, Jin L, Kuntz KW, Pollock RM, Richon VM, et al. The Y641C mutation of EZH2 alters substrate specificity for histone H3 lysine 27 methylation states. *FEBS Lett* 2011;585:3011–4.
62. Kim J, Lee Y, Lu X, Song B, Fong KW, Cao Q, et al. Polycomb- and methylation-independent roles of EZH2 as a transcription activator. *Cell Rep* 2018;25:2808–20.
63. Martinvalet D, Zhu P, Lieberman J. Granzyme A induces caspase-independent mitochondrial damage, a required first step for apoptosis. *Immunity* 2005;22:355–70.

Cancer Research

The Journal of Cancer Research (1916–1930) | The American Journal of Cancer (1931–1940)

Epigenetic Control of *Cdkn2a.Arf* Protects Tumor-Infiltrating Lymphocytes from Metabolic Exhaustion

Brian Koss, Bradley D. Shields, Erin M. Taylor, et al.

Cancer Res Published OnlineFirst October 1, 2020.

Updated version	Access the most recent version of this article at: doi: 10.1158/0008-5472.CAN-20-0524
Supplementary Material	Access the most recent supplemental material at: http://cancerres.aacrjournals.org/content/suppl/2020/10/01/0008-5472.CAN-20-0524.DC1

Visual Overview	A diagrammatic summary of the major findings and biological implications: http://cancerres.aacrjournals.org/content/early/2020/10/02/0008-5472.CAN-20-0524/F1.large.jpg
------------------------	---

E-mail alerts	Sign up to receive free email-alerts related to this article or journal.
Reprints and Subscriptions	To order reprints of this article or to subscribe to the journal, contact the AACR Publications Department at pubs@aacr.org .
Permissions	To request permission to re-use all or part of this article, use this link http://cancerres.aacrjournals.org/content/early/2020/10/02/0008-5472.CAN-20-0524 . Click on "Request Permissions" which will take you to the Copyright Clearance Center's (CCC) Rightslink site.